Journal of Photochemistry and Photobiology 12 (2022) 100142

Contents lists available at ScienceDirect

Journal of Photochemistry and Photobiology

journal homepage: www.sciencedirect.com/journal/journal-of-photochemistry-and-photobiology

Fabrication, characterization, and photovoltaic performance of titanium dioxide/metal-organic framework composite

Phuti S. Ramaripa [a], Kwena D. Modibane [a,*], Katlego Makgopa [b], Ostar A. Seerane [b], Manoko S. Maubane-Nkadimeng [c], Edwin Makhado [a], Mpitloane J. Hato [a], Morongwa E. Ramoroka [d], Kerileng M. Molapo [d], Deepanraj Balakrishnan [e], Emmanuel I. Iwuoha [d]

[a] Nanotechnology Research Group, Department of Chemistry, School of Physical and Mineral Sciences, University of Limpopo (Turfloop), 0727 Polokwane, Sovenga, South Africa
[b] Department of Chemistry, Faculty of Science, Tshwane University of Technology (Arcadia Campus), 0001 Pretoria, South Africa
[c] DSI-NRF Centre of Excellence in Strong Materials, School of Chemistry, University of Witwatersrand, Private Bag X3, Wits, 2050, Johannesburg, South Africa
[d] SensorLab, Chemical Science Department, University of the Western Cape, 7535,Bellville, Cape Town, South Africa
[e] Department of Mechanical Engineering, College of Engineering, Prince Mohammad Bin Fahd University, 31952, Al-Khobar, Saudi Arabia

ARTICLE INFO

Keywords:
Electrochemistry
Metal-organic frameworks
Composite
Titanium dioxide
Photovoltaic studies

ABSTRACT

The titanium dioxide-metal-organic framework (TiO_2_MOF) composite was prepared using the sol-gel method for photovoltaic applications. Raman analyses showed the presence of MOF clusters in the TiO_2 sol-gel network. Using the Brunauer-Emmett-Teller method, the resultant composite material exhibited a surface area of 111.10 $m^2\,g^{-1}$ as compared to the surface area values of 262.90 and 464.76 $m^2\,g^{-1}$ for TiO_2 and MOF, respectively. The small optical band gap values of 2.63 for direct electronic transition and 2.70 eV for indirect allowed electronic transition in TiO_2/MOF composite were observed using ultraviolet-visible supported by cyclic voltammetry (CV). The chronoamperometry (CA) results showed the current drop of 0.21 mA observed at 0.025 s for TiO_2 and the current drop of1.00 mA for MOF and 1.4 mA for TiO_2_MOF composite at 0.3 s. The stability of the composite was achieved through the synergistic effect of MOF on TiO_2 which resulted in a high current density. Electrochemical impedance spectroscopy showed a fast electron transfer as well as high ionic conductivity. The overall power conversion efficiency of 0.722% along with a photocurrent density of 0.46 mA cm^{-2} was achieved for the composite. The approach proposed in this work is facile and can be used for the large-scale fabrication of efficient and flexible photoanode electrodes for photovoltaic applications.

1. Introduction

Globally, there has been a dynamic change in the energy outlook over the years due to the negative environmental impact associated with the use of fossil fuels and the exponential growth in technologies (i.e., optoelectronic applications such as touch screens, solar modules, and photodetectors and electric vehicles). These factors have fostered the development of clean, diversified, sustainable, and low-cost renewable energy systems (i.e., photovoltaic solar cells, wind turbines, etc.) to become valuable for energy provision and technological sustainability [1, 2]. The use of solar power to produce clean energy is made possible through the *R&D* of smart materials to be fabricated into photovoltaic (PV) devices. Photovoltaic devices harness the sun's radiation directly into electricity using the photovoltaic effect [3]. There are several types of solar cells which include perovskite solar cells, organic solar cells, inorganic solar cells, silicon solar cells, dye-sensitized solar cells (DSSC) [4–10], etc. Among these types of solar cells, DSSC is regarded as a potential alternative technology [4], due to its low cost, easy fabrication, and relatively high efficiency. The first work concerning PVs was first reported by Gratzel and O'regan in 1991, which employed the use of DSSC in the production of electric energy from the energy package of light [5]. The effective operation and efficiency of DSSC depend on the type of semiconductors employed. The semiconductors should possess a smaller energy bandgap to facilitate the photo-excited electrons arising from moderate or low energy photons efficaciously for power energy conversion (PEC) [8–10]. For a while, titanium dioxide, TiO_2 has been

* Corresponding author.
E-mail address: kwena.modibane@ul.ac.za (K.D. Modibane).

https://doi.org/10.1016/j.jpap.2022.100142

Available online 30 August 2022

employed as a photoanode used in the DSSCs due to some of its favorable properties in photovoltaic studies such as high chemical and optical stability, non-toxicity, low cost, and corrosion resistance [11–14]. TiO_2 materials can be prepared in several methods such as physical vapor deposition, chemical vapor deposition, hydrothermal, solvothermal and sol-gel methods [12–17]. Among these methods, sol-gel method is more convenient and it produces TiO_2 materials with high purity, homogeneity, felicity, and flexibility [15,17]. There are three commonly known phases of TiO_2 (i.e., rutile, brookite, and anatase) found in nature. Amongst the three, anatase was found to be the most stable form of TiO_2 in the nano-sized particles, even though rutile is the most thermodynamically stable form [11]. Qin et al. [13] reported that porous pure anatase possesses a high surface-to-volume ratio, which is coupled with the surface charge density and has an n-type junction. This has made pure TiO_2 (with its several features) a good candidate for photovoltaic applications with a power conversion efficiency (PCE) of 5.5% [15]. Nonetheless, TiO_2 has high electron recombination of photo-excited electrons and weakly absorbs in the visible regions of the spectra [16]. It has been shown that coating the surface of titanium particles with a nanoscale-thick layer of metal-organic frameworks (MOFs) results in a substantial increase in open-circuit voltage due to inhibited interfacial charge recombination in dye-sensitized solar cells [17–20]. In particular, MOFs have emerged as next-generation materials for various applications (including DSSC) due to their tailorable porosity, large specific surface area, rich redox metal centers, and tunable chemistry (organic linker or metal centers). MOFs are sponge-like crystalline materials made by combining the organic groups through strong bonding components known as organic linkers [19]. Molecular engineering and advancing synthetic technologies have permitted the development of novel MOFs with unique compositions, topologies, and/or architectures, which has resulted in the overwhelming interest in the synthesis of MOFs [20]. Some of the reported synthetic methods include (i) electrochemical synthesis (which was firstly reported in 2005 by researchers at BASF) [20]; (ii) microwave-assisted method (which involves an introduction of energy using microwave irradiation depending on the interaction between electromagnetic waves and electric charges) [21]; (iii) sonochemical synthesis (which uses a high-energy ultrasound to the reaction mixture) [22]; (iv) mechanochemical method (which employs mechanical energy in a chemical reaction) [22]; and (v) solvo/hydrothermal synthesis (which is a commonly known method to prepare MOFs via conventional electric heating in a rector) [21,22]. It was seen that the quality of the crystals obtained by the solvothermal method is similar to those produced by the regular microwave-assisted method [21]. MOFs have been extensively studied for various applications such as heterogeneous catalysis, drug delivery, gas sensing, separation, and storage [23–36]. This is because of their ultra-high surface area, porosity, and tunable functionality [28–32]. Therefore, TiO_2/Cu-MOF composite sol-gel possesses synergetic properties of both TiO_2 and Cu-MOF materials, resulting in a better photovoltaic device. Lee et al. [25] demonstrated the use of a Cu-based MOF decorated with TiO_2 sol-gel (TiO_2–Cu-MOF composite) which achieved the highest PCE of 0.26%. They also showed that the increased power conversion efficiency of TiO_2/Cu-MOF was 0.46% with the addition of carbon nanotubes (CNTs). In another study, the TiO_2/Ru-MOF composite exhibited a power conversion efficiency of 1.22% [26]. Moloto et al. [27] reported that TiO_2-Zn-MOF with current-potential curves and photocurrent density of 1.01 mA cm^{-2} as well as photo-efficiency of 0.67%. It is noteworthy to investigate the feasibility of Cu-based MOF on a TiO_2 surface in a solar cell. Previous studies demonstrated the thin film of ruthenium-based MOFs is synthesized using a layer-by-layer technique in a TiO_2-based liquid junction solar cell [26]. Herein, we report on the synthesis of a TiO_2–Cu-MOF composite prepared using the sol-gel method and used for the first time as a photoanode which demonstrated an enhanced efficiency when fabricated into a photovoltaic device. The weight percentage of the MOF loading was 10 wt.% of the titanium precursor. The interaction between TiO_2 sol-gel and Cu-MOF was confirmed through X-ray diffraction (XRD), Fourier-transform infrared spectroscopy (FTIR), thermogravimetric analysis (TGA), differential thermal analysis (DTA), Raman spectroscopy, transmission electron microscopy (TEM), scanning electron microscopy (SEM) and Brunauer-Emmett-Teller (BET) method. It was discovered that the overall optical absorption was improved using TiO_2–MOF composites. Furthermore, the effects of combining Cu-MOF and TiO_2 sol-gel on photovoltaic performance were investigated via photocurrent response density measurements and electrochemical impedance spectroscopy (EIS). The fabricated solar cells achieved a maximum PCE of 0.722%, which was due to the synergistic effects of increased photocurrent density, faster electron transport, and reduced charge recombination.

2. Experimental section

2.1. Materials

Copper nitrate trihydrate ($CuH_6N_2O_9$) ($\geq$ 99% unadulterated), titanium (IV) tetraisopropoxide (TTIP) ($\geq$ 99% unadulterated), trimesic acid (H_3BTC, $\geq$ 98%), sodium hydroxide (NaOH), acetic acid (glacial), 1-methyl-2-pyrrolidinone, nickel foam substrate, 0.5 mol L^{-1} lithium iodide, copper nitrate, and chloroplatinic acid hydrate (H_2PtCl_6) were purchased from Sigma Aldrich, South Africa. Acetonitrile, dimethylformamide (DMF), ethylene glycol, 2-propanol, and 1-octanol were purchased from Merck, South Africa. The parafilm plastic film was obtained from Bemis, South Africa. Acetic acid, acetyl acetate, ethanol (EtOH), and methanol were purchased from Rochelle Chemicals, South Africa.

2.2. Synthesis of TiO_2/MOF composite

A copper-based MOF was synthesized by following the reported hydrothermal procedure of Ramohlola et al. [32]. Concisely, 4.5 mmol of $Cu(NO_3)_2{\cdot}3H_2O$ in hot distilled water was mixed with 2.5 mmol of H_3BTC (1,3,5 tricarboxylic acid benzene/trimesic acid) in hot ethanol. The subsequent mixture was placed in an autoclave and then subjected to a heating treatment for 36 hrs in an oven at 120 °C. The TiO_2 and TiO_2–MOF composite were prepared using a sol-gel synthetic procedure [15,17,27] with some modifications. Titanium isopropoxide (TTIP) was stabilized using glacial acetic acid and subjected to hydrolysis with deionized water. The titanium solution was stirred vigorously for 1 hr. In the case of TiO_2–MOF composite, about 10 wt.% of MOF to TIP was added to the titanium sol and the mixture was stirred for 2 hrs and adjusted to pH 5 using a 25% ammonia solution to initiate the condensation process. The solution was then left for 24 hrs at 50 °C and after cooling, the solution was filtered and dried at room temperature for 24 hrs to yield 8.54 g of the desired product.

2.3. Electrode preparation

The photovoltaic cells were fabricated according to literature methods [38] with minor modifications. The Ni foam as the substrate was cut into 1 cm × 1 cm dimensions and pasted with a slurry prepared from the photoanode materials (i.e., TiO_2, MOF, and TiO_2–MOF composite). The slurry was prepared by mixing and grinding 1.00 g of TiO_2, MOF, or TiO_2–MOF composite with 0.0005 g of polyvinylidene fluoride (PVDF) and 0.30 mL of 1-methyl-2-pyrrolidinone (NMP) in a quartz pestle and mortar [39]. The electrochemical evaluation (CV, EIS, and CA) of the prepared electrodes was done in a three-electrode cell configuration (0.1 M Na_2SO_4 as electrolyte) using the Biologic instrument (VMP300, EC-lab software) in a temperature-controlled environment at 25 °C. The photocurrent density (I–V curves) was measured at a potential range of 0.3–1.0 V under light conditions at a scan rate of 0.10 Vs^{-1} using a solar simulator equipped with a halogen lamp (potential = 12 V, power = 20 W, power density = 64 mW m^{-2}, Germany, to determine the photocurrent response of the photoanode materials). The

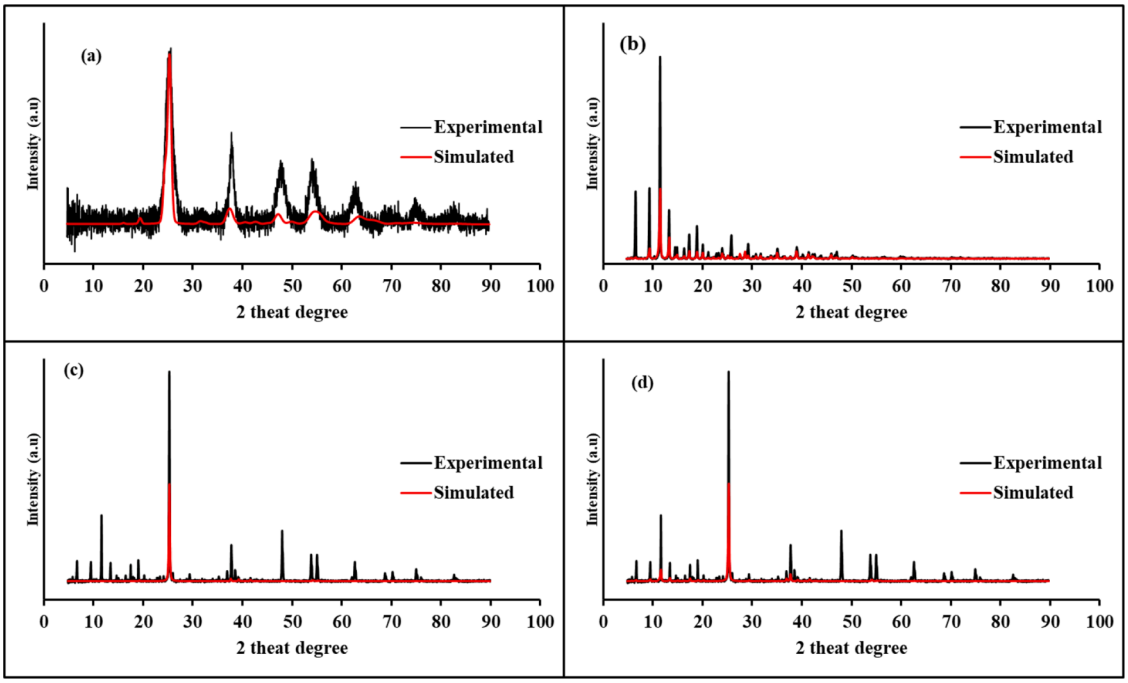

Fig. 1. Experimental and simulated XRD patterns for (a) TiO_2 and (b) MOF. XRD patterns of TiO_2–MOF experimental and simulated with TiO_2 (c) and MOF (d) patterns.

EIS was performed at a frequency range from 0.1 Hz to 100 kHz with an open circuit potential (the Z-fit tool was used for EIS data fitting analysis), and CA analysis was measured at a current density of 2.0 A g^{-1}.

2.5. Characterization technique

Electronic absorption spectra of the materials were documented using a wavelength range of 300 nm – 900 nm over a single front lens at moderate temperatures of around 25 °C utilizing a UV–vis spectrophotometer under ethanol. Structural studies of TiO_2–MOF composite and its precursors were carried out using XRD, Phillips 1830 fitted out with a fine focus lens with a wavelength (λ) peak position of 1.54 angstrom, for both qualitative and quantitative analysis. The crystallography information files (CIF) of TiO_2 and MOF were used in order to plot the XRD simulated pattern. The CIF files were introduced to MAUD software and the powder diffraction analyses were taken. An Agilent Cary 600 Series FTIR spectrometer was used for the identification of functional groups to validate the synthesized TiO_2, MOF, and TiO_2–MOF composite. The FTIR spectra were obtained at room temperature in the wavenumber range between 400 and 4000 cm^{-1}. The surface morphology was studied using scanning electron microscopy (SEM on an FEI Nova 600 instrument) performed at 30 kV. To avoid charging the samples, all the samples were carbon-taped and attached onto aluminum and gold/palladium. A Raman analysis (micro-Raman mod; Jobin-Yvon T64000, wavelength = 532 nm) was done at a focal plane of 1.5 μm in diameter. The BET surface area and pore diameter of the synthesized materials were determined using Micromeritics Tristar 300, outgassing the samples at 150 °C for 4 hrs, and gas sorption using liquid nitrogen (−195 °C). The thermal stability of the materials was conducted using a TGA (Perkin Elmer 6000). Prior to the analysis, the sample (10 mg) was heated in an alumina cup at a temperature starting from a range of 35 °C up to a maximum of 800 °Cat a constant heating rate of 10 °C min^{-1}.

3. Results and discussions

3.1. Structural characterization

Fig. 1 shows the XRD patterns for TiO_2, MOF, and TiO_2–MOF composite. The patterns in Fig. 1(a) for TiO_2 show the diffraction peaks at 2θ = 25.0°, 38.3, 48.0, 54.0, and 62.0°, as an indication of the presence of the anatase TiO_2 phases for the hkl indexes of (101), (004), (200), (105) and (204) corresponding to the simulated pattern (JCPDS no: 21–1272), respectively. The findings are similar to the work reported by Alwin *et al.* [17] and Devi *et al.* [40]. It means that the TiO_2 particles are favorably crystallized in the anatase phase. It was seen that the broad diffraction peaks are owing to the nanosized anatase crystals from the TiO_2 sol-gel network [17]. This was supported by the crystallite size of 16.12 nm for TiO_2 material calculated using the Debye–Scherrer formula from (101) plane using Eq. (1) [36,37].

$$D = \frac{0.9\lambda}{\beta \mathrm{Cos}\theta} \tag{1}$$

where β represents the full-width at half-maximum (FWHM) measured in radians, λ for the X-ray wavelength of Cu-Kα radiation, which is 1.5406 Å, and θ stands for the Bragg's angle. In addition, the calculated D-spacing ($2d\sin\theta = n\lambda$) for 101 hkl value was 3.48 Å for TiO_2.

It is noticeable that MOF has an octahedral crystal structure similar to the simulated one from crystal structure information data (CSID) (Fig. 1(b)). This shows that the structural phases of MOF known as HKUST-1 were well-maintained with high purity [28–32]. Furthermore, MOF showed well-defined sharp peaks as an indication of a highly crystalline compound [33–35]. The intense patterns were indexed at 2θ = 6.9, 9.2, 11.50, 13.27 and 18.85° for (200), (220), (222), (400) and (440) planes [33–35], respectively. It was seen at lower 2θ that the intense peaks were characteristics of a microporous material, which had several tiny pores or cavities [28–35]. This was also supported by the crystallite size of 99.76 nm for MOF material calculated using the Debye–Scherrer formula from (222) plane and D-spacing of 7.69 Å. On the other hand, the diffraction peaks emanating from the TiO_2 spectrum were noticed in the TiO_2MOF composite as shown in Fig. 1(c) by a

Table 1
BET parameters, optical and electrochemical properties of TiO_2, MOF and TiO_2/MOF nanocomposite.

Material	BET Surface area (m^2g^{-1})	Pore width (nm)	Optical Bandgap (eV)[a]	$E^{Ox}_{1/2}$ (V)	$E^{red}_{1/2}$ (V)	E_{HOMO} (eV)	E_{LUMO} (eV)
Ni foam	–	–	–	0.40	0.35	−5.1	−4.35
TiO_2	262.90	2.66	3.15	0.41	0.33	−5.08	−4.34
MOF	464.76	2.56	2.96	0.63	0.50	−5.25	−4.12
TiO_2_MOF	111.10	3.40	2.63	0.47	0.24	−4.99	−4.28

[a] Optical bandgap using direct allowed transition.

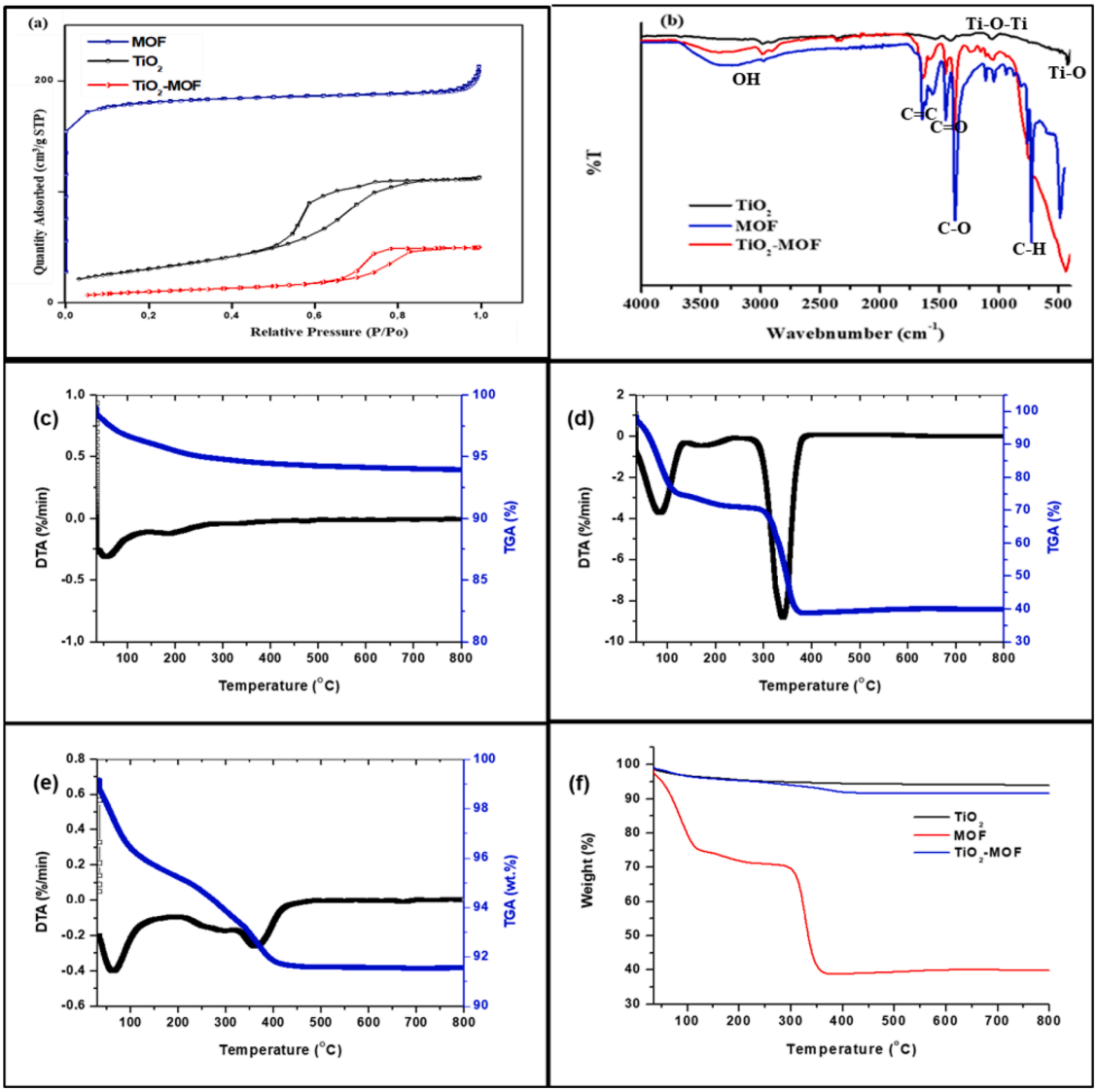

Fig. 2. (a) BET plots and (b) FTIR of TiO_2, MOF, and TiO_2_MOF composite; (c) DTA-TGA curves of TiO_2; (d) DTA-TGA curves of MOF; (e) DTA-TGA curves of TiO_2_MOF; and (f) TGA of TiO_2, MOF and TiO_2_MOF composite.

simulated TiO_2 pattern. The TiO_2MOF composite phases were shown by the most crystalline peak at $2\theta = 25.0^\circ$ for the 101 hkl index of the TiO_2 phase [17]. Moreover, the peaks originated from MOF in the pattern of TiO_2_MOF composite (Fig. 1(d)) were also simulated and indexed at 2θ = 6.9, 9.2, 11.62, and 13.27 ° for (200), (220), (222), and (400) [33–35]. It was seen that the MOF has not affected the anatase phase formation of TiO_2 crystals during synthesis [15,17]. The crystallite size of the TiO_2_MOF composite was found to be 123.41 nm with a D-spacing of 3.52 Å, which is consistent with the reported TiO_2 sol-gel composites [17,27]. The amount of MOF crystallinity in the TiO_2_MOF composite was estimated from its phase intensity by applying Vegard's law and found to be 9.031 wt.%.

In XRD, the lattice strain ($\varepsilon = \beta\cos\theta/4$) and dislocation density ($\rho = 1/D^2$) of the TiO_2, MOF, and TiO_2_MOF composite can be determined from full-width at half-maximum, and crystallite size. The lattice strain in TiO_2, MOF, and TiO_2_MOF composite was found to be 21.5×10^{-4}, 3.47×10^{-4}, and 2.81×10^{-4}, respectively. This indicates a reduction of lattice strain upon composite formation. The ρ values were estimated to be 38.46×10^{14} lines m^{-2} for TiO_2 and with a reduction dislocation density of 0.6646×10^{14} lines m^{-2} for composite and 1.0146×10^{14} lines m^{-2} for MOF. The lower ρ value of TiO_2_MOF indicates that the composite has a high degree of crystallinity as compared to TiO_2 due to the presence of MOF as an indication of a suitable material for photovoltaic solar cells

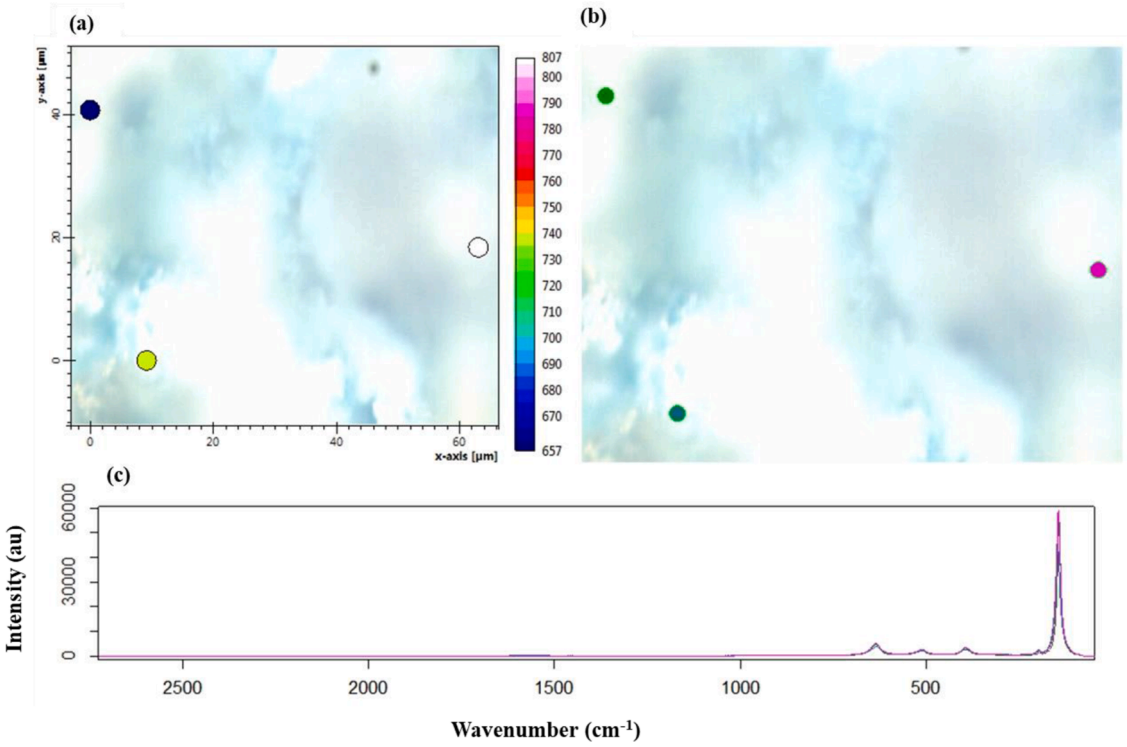

Fig. 3. Raman images (a) and (b) and spectra (c) of TiO_2/MOF composite.

The BET results for surface area and porous structure obtained from nitrogen adsorption measurements were evaluated at 77 K are listed in Table 1 and given in Fig. 2(a). The specific surface area of the TiO_2_MOF composite was found to be 111.10 $m^2 g^{-1}$, which was lower than the one of TiO_2 (262.90 $m^2 g^{-1}$) and MOF (464.76 $m^2 g^{-1}$). The addition of 10% MOF has a substantial change in the surface area of the composite due to the formation of agglomerates [34,35] and MOF occupying the pores of the TiO_2 network [17]. It was demonstrated that the MOF clusters may be attached to the surface of the sol-gel network and either increase the surface area or be left unchanged depending on the surface area of the MOF [17]. However, the pore width in the composite was observed to be a bit higher as compared to TiO_2 due to the introduction of MOF. The surface area and pore width observed in the TiO_2_MOF composite indicates that the composite can have an influence on a carrier transport in solar cells.

Fig. 2(b) shows the FTIR spectra for TiO_2, MOF, and TiO_2_MOF composite. In the spectrum of TiO_2, the characteristic anatase TiO_2 is confirmed by the peaks at 627 cm^{-1} and 1404 cm^{-1}, which are ascribed to the Ti-O stretching vibration and Ti-O-Ti stretching vibrations, respectively. The FTIR spectrum of MOF shows two small peaks at 731 and 761 cm^{-1} that corresponds to in-plane and out-of-plane C—H bending modes on the benzene ring in MOF [28–30]. The strong peak at 1371 cm^{-1} is due to the vibrational mode of the R-C-O stretch of Cu-MOF [33]. The peaks at 1489 and 1550 cm^{-1} are assigned to the symmetry and asymmetry vibrational modes of C=O of carboxylate groups in both MOF and composite [34,35]. The peak at 1645 cm^{-1} attributed to the C=C vibrational of the benzene ring in MOF was observed [31,32]. After the formation of the TiO_2_MOF composite, a broad peak in the region of 400 – 1000 cm^{-1} is due to the vibrational mode of the Ti-O stretching bond [40]. The weak peaks at 2200 and 2400 cm^{-1} are attributed to TiO_2 asymmetric in both TiO_2 and composite [40,41]. The broad peaks in the region of 3000 and 3400 cm^{-1} are assigned to the vibrational modes of Ti-OH of TiO_2 and OH that show the existence of hydrated Cu-MOF [41,28]. Both TiO_2 and MOF vibrational modes were observed in the TiO_2_MOF composite spectrum as an indicative of composite formation. Fig. 2(c)–(f) shows the TGA and differential thermal analysis (DTA) for TiO_2, MOF, and TiO_2_MOF composite. In Fig. 2(c), the TGA curve of TiO_2 shows one small degradation step that is due to the loss of moisture and this suggests the stability of TiO_2 while the DTA curve shows one small exothermic peak of TiO_2. This is in contrast with Zoccal et al. [42], where they observed two degradation steps which are due to the loss of water and pyrolysis. Fig. 2 (d) shows the TGA curve with the two main degradation steps of MOF. The first degradation step corresponds to the loss of water and ethanol, and the second degradation step corresponds to the loss of organic linker and the product remains with CuO. The DTA curve in Fig. 2(d) agrees with the TGA and shows the two main exothermic peaks [32]. Fig. 2(e) shows two small degradation steps, which correspond to the loss of water and organic linker of MOF in the composite. This indicates the presence of MOF in the TiO_2_MOF composite. In addition, the DTA curve in Fig. 2(e) shows the two small exothermic peaks. Therefore, the TGA curves in Fig. 2(f) suggest the improvement in the thermal stability of the TiO_2_MOF composite as compared to MOF.

This was further confirmed by Raman's analysis of the TiO_2_MOF composite as represented in Fig. 3 which shows the Raman images (a and d) and spectra (c) of the TiO_2_MOF composite. The strong vibrational mode in the composite around 140 cm^{-1} is assigned to the symmetric stretching vibration of a single crystal (Eg) for O-Ti-O in TiO_2 [41]. Three weak vibration modes at a wavenumber of 399 cm^{-1} (B1g), 513 cm^{-1}(A1g), and 639 cm^{-1} (Eg) are caused by the antisymmetric bending vibration of O-Ti-O [40,41]. The vibrational modes at 193–172 cm^{-1} for MOF in the composite were observed due to the presence of Cu-O and Cu-Cu stretching modes [43]. The vibrational mode in the region of 790–810 cm^{-1} for composites is attributed to the C—H of the aromatic ring stretching mode of the MOF component [32]. Furthermore, the 1450–1510 cm^{-1} region in the composite shows the presence of C=O attached to the aromatic ring in MOF [32].

Fig. 4(a) shows a pure TiO_2 smooth granule shape [40]. As shown in Fig. 4(b), MOF displays usual irregular crystals which possess octahedral shapes with smooth surfaces [28]. The intervention of TiO_2 and MOF is shown in Fig. 4(c), which shows uniformly arranged particles with an irregularly shaped aggregate on the surface. The particles are well

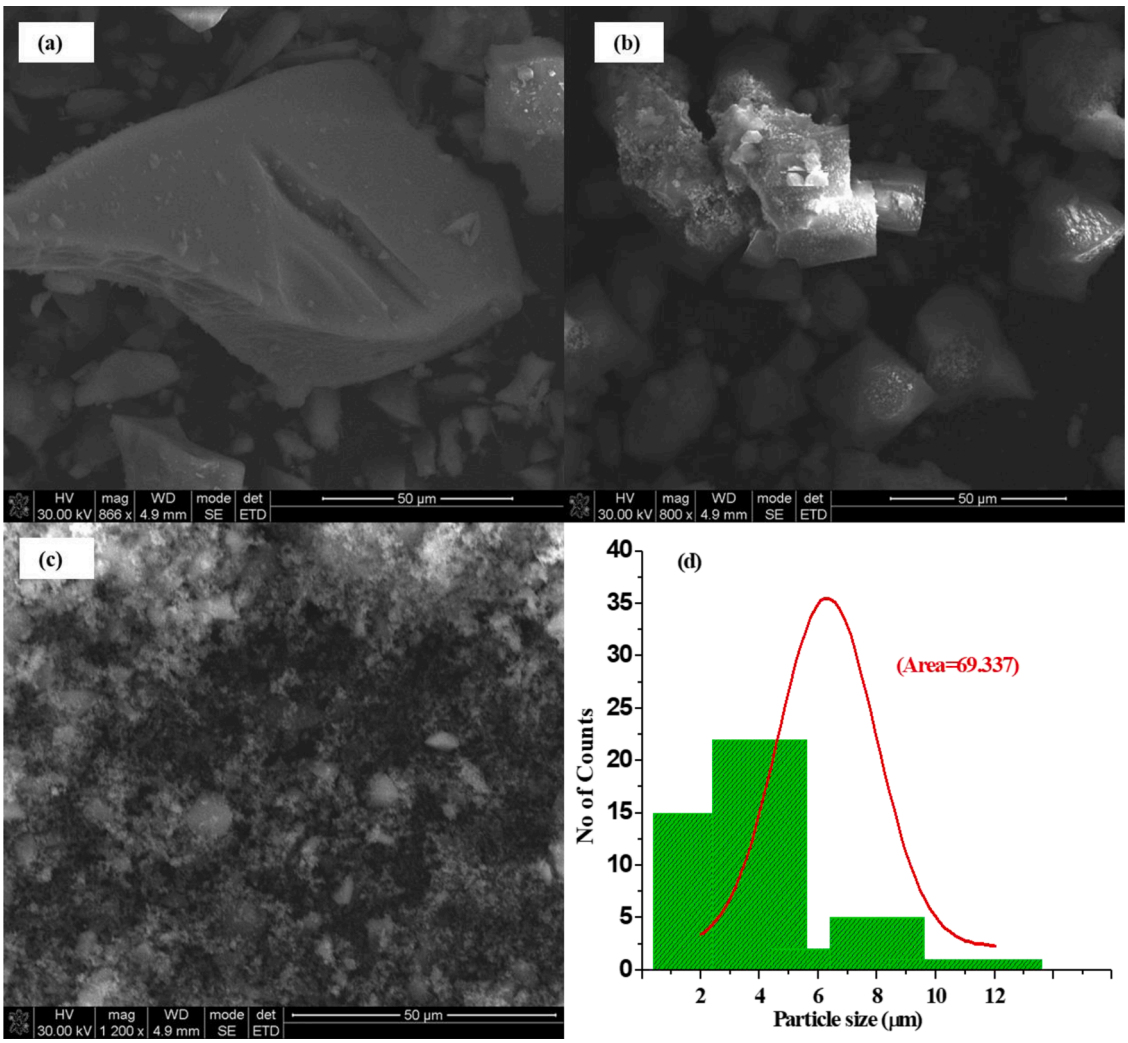

Fig. 4. SEM images of (a) TiO_2, (b) MOF, and (c) TiO_2/MOF; and (d) particle size distribution of TiO_2/MOF.

interconnected with each other and form a continuous network structure. The appearance was similar to the TiO_2-Zn-MOF reported by Alwin *et al.* [17]. It is noteworthy to indicate that the network structure of the TiO_2–MOF composite is highly porous and the porous morphology is visible from the SEM image (Fig. 4(c)). It is also well-known from the image that the microporous MOF clusters are attached to the surface of the TiO_2 network [17].

In addition, it was seen that the continuous arrangement of the pore-solid network was also evident from the SEM image with major particle sizes ranging between 4 and 6 µm (Fig. 4(d)). The fitted surface area from particle size distribution was found to be 69.337 $m^2 g^{-1}$ which was supported by the BET analysis above.

3.2. Optical characterization

The UV-visible spectra of TiO_2, MOF, and TiO_2–MOF composite are presented in Fig. 5(a). The TiO_2 shows an absorption maxima at 342 nm which corresponds to the D-d transition of TiO_2 [17]. The MOF has an absorption band at 357 nm, which is attributed to the ligand-to-metal charge transfer [43]. Remarkably, different metal ions and ligands in MOF have varied interactions and distinct optical absorption, which make them suitable photocatalysts [43,44]. The introduction of MOF on the TiO_2 surface resulted in a redshift of the D-d transition of TiO_2 due to light-harvesting of MOF [44]. It was reported that the absorption of a photon with energy equal to or greater than the bandgap results in the excitation of an electron from the valence to the conduction band, leaving a hole in the valence band [45]. The generation of an electron-hole pair within the same molecule corresponds to the optical bandgap energy [45]. Based on the UV–vis spectra (Fig. 5(a)), the optical bandgap energies were determined using the Tauc plot by Eq. (2) [36,37,38]:

$$\alpha h\nu(\nu) = \beta(h\nu - Eg)^n \quad (2)$$

The assumturity coefficient is represented as α; frequency of light as ν; and β for the bandgap tailing parameter. The plank constant and optical band gap energy is represented as h and Eg, respectively. The n symbol in Eq. (2) represents the transition probability index for direct and indirect allowed electronic transitions with n values of 1/2 and 2, respectively. The Eg values were presented in Fig. 5(b,c) and (d) for direct and indirect allowed electronic transition of TiO_2, MOF, and TiO_2/MOF composite. The composite has been shown to have a small bandgap of 2.63 and 2.70 eV for direct and indirect allowed electronic transitions (Fig. 5(d) and Table 1). The smaller bandgap energy of TiO_2/MOF material indicates that there are some new electronic states between the valence and conduction bands of TiO_2 [17]. It was also shown the smaller bandgap increases the photoactivity of the material in a wider range of solar spectrum which is favorable to achieving better performance in a photovoltaic cell.

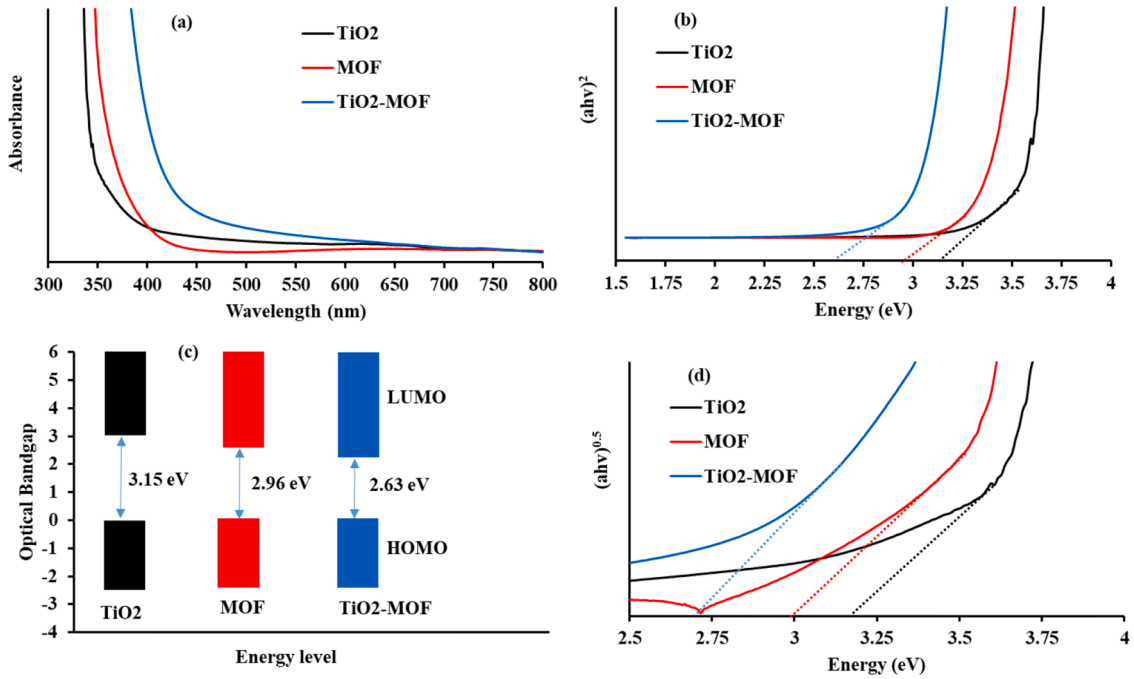

Fig. 5. (a) UV–vis spectra of TiO_2, MOF and TiO_2/MOF nanocomposite; and (b) their respective optical energy band gap using the (c) direct and (d) indirect allowed electronic transitions.

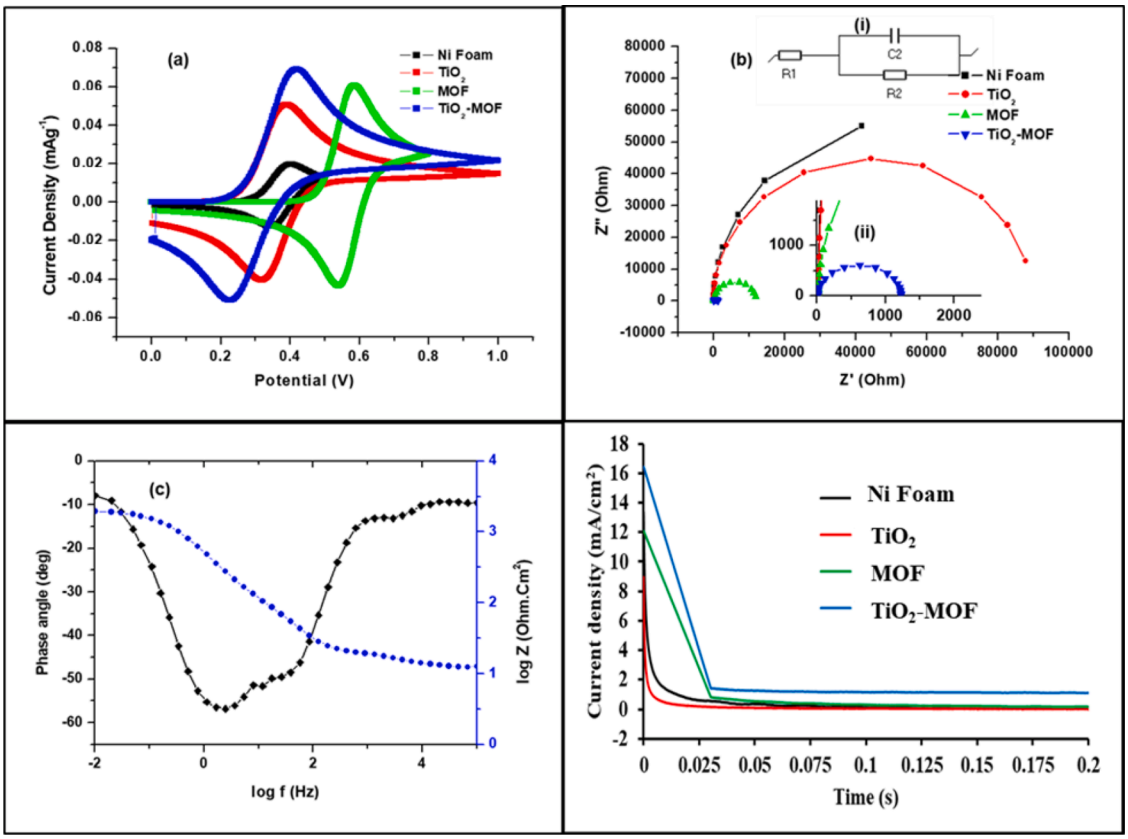

Fig. 6. (a) Cyclic voltammograms (at scan rate 0.10 V s^{-1}) and (b) Nyquist plots, of bare Ni foam, TiO_2, MOF, and TiO_2–MOF composite (Inset: (i) equivalent circuit and (ii) enlargement area); (c) Bode plot of TiO_2–MOF composite; and (d) chronoamperometry curves of bare Ni foam, TiO_2, MOF and TiO_2–MOF, in 0.1 M Na_2SO_4 electrolyte.

Table 2
Fitted circuit parameters of EIS of Ni foam, TiO_2, MOF and TiO/MOF composite and calculate ionic conductivity.

Material	Electrolyte	Rs (Ω)	CPE (μF)	Rct (kΩ)	Conductivity (μS/cm)
Ni foam	0.1 M Na_2SO_4	19.7	184	114	0.9
TiO_2	0.1 M Na_2SO_4	23.3	25.7	89.6	1.1
MOF	0.1 M Na_2SO_4	21.3	153	11.9	8.4
TiO_2_MOF	0.1 M Na_2SO_4	15.3	172	1.21	82.6

3.3. Electrochemical characterization

It is well known that the electron injection into a neutral molecule (first reduction process) and electron extraction from a neutral molecule (first oxidation process) are electrochemically determined using CV [45]. Fig. 6(a) shows the overlaid cyclic voltammograms of bare Ni foam (blank), TiO_2, MOF, and TiO_2_MOF composite. The potential for the first ring oxidation and reduction, $E_{1/2(ox)}$ and $E_{1/2(red)}$, respectively are listed in Table 1. From these values, the highest occupied molecular orbital (E_{HOMO}) energy levels were calculated according to Data *et al.* [46] using Eq. (3):

$$E_{HOMO} = -\left(E_{1/2(red)} + 4.75\right)\ eV \quad (3)$$

The E_{HOMO} values were found to be −5.10, −5.08, −5.25, and −4.99 eV for bare Ni foam, TiO_2, MOF, and TiO_2_MOF nanocomposite, respectively. A significant lowering of E_{HOMO} was observed due to an increase in the electronic properties of the composite caused by the addition of MOF. On the other hand, the lowest unoccupied molecular orbital (E_{LUMO}) values are determined using Eq. (4) [46,47]. In this work, the E_{LUMO} values were calculated using Eq. (4) and found to be −4.35, −4.34, −4.12, and −4.28 eV for bare Ni foam, TiO_2, MOF, and TiO_2_MOF composite, respectively.

$$E_{LUMO} = -\left(-E_{1/2(ox)} + 4.75\right)\ eV \quad (4)$$

The EIS is usually used to examine the dynamics of electron transport and recombination across interfaces [33]. Fig. 6(b) shows the Nyquist plots of the bare Ni foam, TiO_2, MOF, and TiO_2_MOF composite, the experimental data were fitted using the Z-fit software according to the electrical equivalent circuit. It comprises Voigt RC elements, involving a solution/electrolyte resistance (Rs denoted as R1), charge-transfer resistance (Rct denoted as R2), and constant phase elements (CPE or Q denoted as C2) as shown by inset (i) in Fig. 6(b). The diameter of the semicircle from the Nyquist curve provides information about the R_{ct}. As seen in Fig. 6(b), the semicircle of TiO_2_MOF composite (inset (ii)) is smaller than the one of TiO_2 material, which suggests the reason for enhanced electrochemical properties caused by MOF. The values of the fitted EIS parameters are summarized in Table 2. The Rs value decreased with the introduction of MOF content as compared to TiO_2 material from 23.32 Ω to 15.3 Ω in the composite. This indicates that the composite provides better contact with the Ni foam substrate which results in improved electronic performance than pristine TiO_2 [17]. The total ionic conductivity (δ) is estimated from the charge-transfer resistance (R_{ct}) using the thickness (t) and the cross-sectional area (A) by the following relation in Eq. (5).

$$\delta = t/(R_{ct}A) \quad (5)$$

The total ionic conductivity of Ni foam, TiO_2, MOF, and TiO_2_MOF nanocomposite was found to be 0.9, 1.1, 8.4, and 82.6 μS/cm, respectively. The lower value of ionic conductivity observed in bare Ni foam and TiO_2 was due to high charge-transfer resistance, because it limits the total ionic conductivity in the materials. It was seen that the introduction of MOF increased the ionic conductivity. The comparison of the results obtained in this work with the previous reports in the literature is presented in Table 2, which shows that the ionic conductivity obtained in this work is in good agreement with the values reported previously [33]. In addition, a logarithmic of impedance and phase angle are both plotted as a function of logarithmic frequency to give a Bode plot. The phase angle vs log frequency curve of the TiO_2_MOF composite (Fig. 6 (c)) shows a broad peak and the peak height is proportional to the charge-transfer resistance response. The lower charge-transfer resistance values occurring at the higher frequency indicate that the TiO_2_MOF composite possesses a high ionic conductivity as observed in the Nyquist plot. The lifetime (τ) of the composite was estimated from a maximum peak frequency (f_{max}) of 57.5 using Eq. (6) [48] and it was found to be 2.77 ms.

$$\tau = 1/(2\pi f_{max}) \quad (6)$$

Furthermore, the chronoamperometric method was used to investigate the electrochemical stability of bare Ni foam, TiO_2, MOF, and TiO_2_MOF composite which involves measuring current as a function of time and controlling the voltage. The chronoamperometric current time response curves are presented in Fig. 6(d). A well-defined chronoamperometric response was seen on the curve for all materials with a high current at the initial stage. A current drop in the chronoamperometry curve of 0.50 mA was observed at 0.025 s for Ni foam and a fast drop in TiO_2 of 0.21 mA. The current drops of 1.00 and 1.40 mA were observed at 0.3 s for MOF and TiO_2/MOF composite, respectively. It was seen that the introduction of MOF resulted in a high current density of 1.4 mA which denotes the stability of the electrode surface [10]. It was seen in this work that the tested current remained constant for such a long time to indicate the better stability of the composite.

The photocurrent densities of the prepared Ni Foam, TiO_2, MOF, and TiO_2_MOF composite were obtained from the cathodic cyclic voltammetry scan conducted on the photoanodes in simulated light (64 mW m^{-2} intensity), and the results are given in Fig. 7(a). It was shown that Ni foam, TiO_2 and MOF materials possessed photocurrent densities of 0.02 (at 0.38 V), 0.39 (at 0.31 V) and 0.19 (at 0.66 V) mA cm^{-2}. The low photocurrent is ascribed to the poor light absorption resulting from the

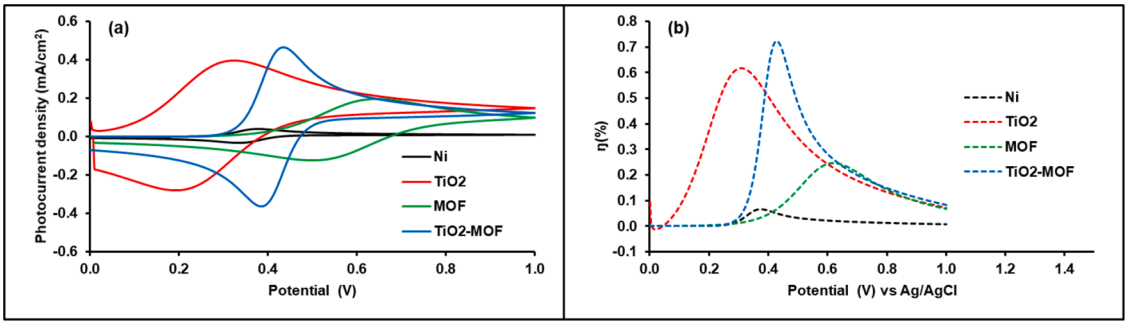

Fig. 7. (a) Photocurrent response and (b) power conversion efficiency of Ni foam, TiO_2, MOF, and TiO_2_MOF composite.

Table 3
Comparison of the photocurrent density obtained for Ni foam, TiO_2, MOF, and TiO_2_MOF composites in this study with the literature values prepared using various methods.

Material	Electrolyte	Photocurrent (mA/cm^2)	Efficiency (%)	Ref
Ni foam	0.1 M Na_2SO_4	0.02	0.066	In this work
TiO_2	0.1 M Na_2SO_4	0.39	0.617	In this work
MOF	0.1 M Na_2SO_4	0.19	0.255	In this work
TiO_2_MOF	0.1 M Na_2SO_4	0.46	0.722	In this work
TiO_2–Cu-MOF	I_3 /I^- redox	–	0.26	[25]
TiO_2–Cu-MOF/CNT	I_3 /I^- redox	–	0.46	[25]
TiO_2-Ru-MOF	I_3 /I^- redox	–	1.22	[26]
TiO_2-Zn-MOF	ACN, LiI, I_2 & $LiClO_4$	1.04	0.67	[27]
Cu-ZnO	0.1 M Na_2SO_4	–	0.062%	[53]

compact nature of the nanoparticles at the material's surface, which caused poor charge separation and reduced photocatalytic efficiency [49]. The maximum photocurrent density of 0.46 mA cm^{-2} at 0.44 V was obtained in TiO_2_MOF materials. The highest photocurrent density attained for the composite was well within the many photoresponses that have been reported for the material under illumination conditions [50–53]. Table 3 compares the maximum photocurrent attained by the Ni, TiO_2, MOF, and TiO_2_MOF materials in this work with other reported values in the literature. The enhanced photocurrent obtained for the TiO_2_MOF composite is largely related to the porous nature of the material's surface, which created a larger area and increased active sites for the electron transfer mechanism, thus enhancing the photocurrent. The power conversion efficiency (η) of the Ni foam, TiO_2, MOF, and TiO_2_MOF composites, was calculated using Eq. (7) [27]:

$$\eta = \left(\left(E^0_{rev} - -E_{mea}\right) \times I\right)/P_{in} \quad (7)$$

where I (mA cm^{-2}) is the measured photocurrent density, E_{mea} is the electrode potential of the working electrode whose photocurrent was tested under irradiation, E^0_{rev} is the standard state-reversible potential (1.43 V Ag/AgCl) of the working electrode, and P_{in} (mW cm^{-2}) is the input power of the simulated light intensity.

The η values estimated for the Ni foam, TiO_2, MOF, and TiO_2_MOF composites are given in Fig. 7(b). The highest and lowest η values were 0.722 and 0.066% for the TiO_2_MOF composite and Ni foam, respectively. The conversion efficiencies of TiO_2 and MOF were 0.617 and 0.255%, respectively. The η values reported in Table 3 for TiO_2_MOF composite are higher than those reported in the literature at 0.26% using TiO_2/Cu-MOF [25], 0.67% using TiO_2/Zn-MOF [27], and 0.46% for TiO_2–Cu-MOF/CNT [25], whereas its efficiency value was less than that of 1.22% using TiO_2-Ru-MOF [26]. However, the results are comparable showing that the Cu-based MOF has the potential to be used to improve TiO_2 properties. The overall power conversion efficiency of 0.722% and photocurrent density of 0.46 mA cm^{-2} for TiO_2_MOF composite were attributed to the increase in the electronic properties of the composite material [17]. It is shown that Cu-BTC MOFs are the best candidates to be employed as stabilizing materials for TiO_2 photoanodes in solar cells. This is due to their simple synthetic route and environmental friendliness as compared to other MOFs. The heterojunction between TiO_2 and Cu-based MOF also improved the thermal stability of the MOFs as shown above. In addition, the TiO_2_MOF composite showed higher performance as compared to zinc oxide doped with copper (Cu-ZnO) film [53] in the same electrolyte of 0.1 M Na_2SO_4 solution.

4. Conclusion

A new class of TiO_2/Cu-based MOF composite was prepared by the sol-gel method and confirmed by XRD, FTIR, Raman, SEM, and BET. The synthesized materials were employed as photoanode materials for photovoltaic solar cells. The XRD pattern of the materials confirmed the phase of the pure MOF and TiO_2 in the TiO_2_MOF composite. Raman and FTIR spectra revealed the vibrations of benzene rings of MOF and Ti-O stretches, further confirming the high purity of the nanocomposite produced. It was found that the thermogravimetric analysis showed an improvement in the thermal stability of the composite. The optical band gap values ranged between 3.15 and 2.63 eV from UV–Vis; and the HOMO-LUMO values using CV were estimated for the TiO_2, MOF, and TiO_2_MOF composites. On the other hand, the EIS showed that the TiO_2_MOF composite possessed high conductivity. These parameters make TiO_2_MOF composite a suitable candidate for photovoltaic solar cell applications. A maximum photocurrent and power efficiency of 0.46 mA cm^{-2} and 0.722% were recorded for the TiO_2_MOF composite under a simulated light source, respectively. The TiO_2_MOF composite was more porous compared to the other films, as revealed by SEM studies, allowing for easier charge separation of photogenerated charge carriers and leading to the improved photocurrent observed. Notwithstanding, the sol-gel method for preparing TiO_2_MOF composite used in this study showed promising photocurrent response and could also be employed for making TiO_2_MOF composite for photovoltaic applications.

Declaration of Competing Interest

We wish to confirm that there are no known conflicts of interest associated with this publication and there has been no significant financial support for this work that could have influenced its outcome. We confirm that the manuscript has been read and approved by all named authors and that there are no other persons who satisfied the criteria for authorship but are not listed. We further confirm that the order of authors listed in the manuscript has been approved by all of us.

We understand that the Corresponding Author is the sole contact for the Editorial process (including Editorial Manager and direct communications with the office). He is responsible for communicating with the other authors about progress, submissions of revisions and final approval of proofs. We confirm that we have provided a current, correct email address which is accessible by the Corresponding Author.

Acknowledgements

K.D.M, MJH, and K.M thank the financial support from the National Research Foundation (NRF) under the Thuthuka programme (UID Nos. 117727, 118113, and 117984) and the Competitive Support for Unrated Researchers (UID No. 138085) programmes.

References

[1] N. Linares, A.M. Silvestre-Albero, E. Serrano, J. Silvestre-Albero, J. García-Martínez, Mesoporous materials for clean energy technologies, Chem. Soc. Rev. 43 (2014) 7681–7717.
[2] P.V. Kamat, Meeting the clean energy demand: nanostructure architectures for solar energy conversion, J. Phys. Chem. C. 111 (2007) 2834–2860.
[3] D.M. Powell, M.T. Winkler, H. Choi, C.B. Simmons, D.B. Needleman, T. Buonassisi, Crystalline silicon photovoltaics: a cost analysis framework for determining technology pathways to reach baseload electricity costs, Energy Environ. Sci. 5 (2012) 5874–5883.
[4] G.R. Timilsina, L. Kurdgelashvili, P.A. Narbel, Solar energy: markets, economics and policies, Renew. Sust. Energ. Rev. 16 (2012) 449–465.
[5] M. Raugei, P. Frankl, Life cycle impacts and costs of photovoltaic systems: current state of the art and future outlooks, Energy 34 (2009) 392–399.
[6] M. Grätzel, Dye-sensitized solar cells, J. Photochem. Photobiol. C 4 (2003) 145–153.
[7] B. O'regan, M. Grätzel, A low-cost, high-efficiency solar cell based on dye-sensitized colloidal TiO_2 films, Nature 353 (1991) 737–740.

[8] A. Hagfeldt, G. Boschloo, L. Sun, L. Kloo, H. Pettersson, Dye-sensitized solar cells, Chem. Rev. 110 (2010) 6595–6663.

[9] M.E. Ramoroka, S.B. Mdluli, V.S. John-Denk, K.D. Modibane, C.J. Arendse, E. I. Iwuoha, Synthesis and photovoltaics of novel 2, 3, 4, 5-tetrathienylthiophene-co-poly (3-hexylthiophene-2, 5-diyl) donor polymer for organic solar cell, Polymers (Basel) 13 (2020) 1–14.

[10] K. Amarsingh Bhabu, A. Kalpana Devi1, J. Theerthagiri, J. Madhavan, T. Balu, T. R. Rajasekaran, Tungsten doped titanium dioxide as a photoanode for dye sensitized solar cells, J. Mater. Sci.: Mater. Electron. 28 (2017) 3428–3439. M.S. Kang, J.H. Kim, J. Won, Y.S. Kang, Oligomer approaches for solid-state dye sensitized solar cells employing polymer electrolytes, J. Phys. Chem. C 111 (2007) 5222–5228.

[11] K. Nemade, P. Dudhe, P. Tekade, Enhancement of photovoltaic performance of polyaniline/graphene composite-based dye-sensitized solar cells by adding TiO_2 nanoparticles, Solid State Sci 83 (2018) 99–106.

[12] F. Chindeka, P. Mashazi, J. Britton, G. Fomo, D.O. Oluwole, A. Sindelo, T. Nyokong, Optimizing phthalocyanine based dye-sensitized solar cells: the role of reduced graphene oxide, Synth. Met 246 (2018) 236–245.

[13] W. Qin, J.J. Liu, S.L. Zuo, Y.C. Yu, Z.P. Hao, Solvothermal synthesis of nanosized TiO_2 particles with different crystal structures and their photocatalytic activities, J. Inorg. Mater. 22 (2007) 931–936.

[14] Y. Li, H. Wang, Q. Feng, G. Zhou, Z.-.S. Wang, Gold nanoparticles inlaid TiO_2 photoanodes: a superior candidate for high-efficiency dye-sensitized solar cells, Energy Environ. Sci. 6 (2013) 2156–2165.

[15] V. Ramasubbu, S. Alwin, E. Mothi, X.S. Shajan, TiO_2 aerogel–Cu-BTC metal-organic framework composites for enhanced photon absorption, Mater. Lett. 197 (2017) 236–240.

[16] S. Ansari, M. Cho, Highly visible light responsive, narrow band gap TiO_2 nanoparticles modified by elemental red phosphorus for photo-catalysis and photo electrochemical applications, Sci. Rep 6 (2016) 25405.

[17] S. Alwin, V. Ramasubbu, X.S. Shajan, TiO_2 aerogel–metal organic framework nanocomposite: a new class of photoanode material for dye-sensitized solar cell applications, Bull. Mater. Sci. 41 (2018) 1–8.

[18] M.C. So, G.P. Wiederrecht, J.E. Mondloch, J.T. Hupp, O.K. Farha, Metal–organic framework materials for light-harvesting and energy transfer, Chem. Commun. 51 (2015) 3501–3510.

[19] R. Kaur, K.H. Kim, A. Paul, A. Deep, Recent advances in the photovoltaic applications of coordination polymers and metal organic frameworks, J. Mater. Chem. A. 4 (2016) 3991–4002.

[20] Y.R. Lee, J. Kim, W.S. Ahn, Synthesis of metal-organic frameworks: a mini review, Korean J. C. Eng. 30 (2013) 1667–1680.

[21] D. Banerjee, C.M. Simon, S.K. Elsaidi, M. Haranczyk, P.K. Thallapally, Xenon gas separation and storage using metal-organic frameworks, Chem 4 (2018) 466–494.

[22] C. Zhu, H. Tang, K. Yang, X. Wu, Y. Luo, J. Wang, Y. Li, A urea-containing metal-organic framework as a multifunctional heterogeneous hydrogen bond-donating catalyst, Cat. Commun. 135 (2020), 105837.

[23] J.T. Joyce, F.R. Laffir, C. Silien, Layer-by-layer growth and photocurrent generation in metal–organic coordination films, J. Phys. Chem. C. 117 (2013) 12502–12509.

[24] Y. Li, A. Pang, C. Wang, M. Wei, Metal–organic frameworks: promising materials for improving the open circuit voltage of dye-sensitized solar cells, J. Mater. Chem. 21 (2011) 17259–17264.

[25] D.Y. Lee, D.V. Shinde, S.J. Yoon, K.N. Cho, W. Lee, N.K. Shrestha, S.H. Han, Cu-based metal–organic frameworks for photovoltaic application, J. Phys. Chem. 118 (2014) 16328–16334.

[26] D.Y. Lee, E.-.K. Kim, C.Y. Shin, D.V. Shinde, W. Lee, N.K. Shrestha, J.K. Lee, S.-H. Han, Layer-by-layer deposition and photovoltaic property of Ru-based metal–organic frameworks, RSC Adv 4 (2014) 12037–12042.

[27] W. Moloto, P. Mbule, E. Nxumalo, B. Ntsendwana, Stabilizing effects of zinc(II)-benzene-1,3,5-tricarboxylate metal organic frameworks on the performance of TiO_2 photoanodes for use in dye-sensitized solar cells, J. Photochem. Photobiol. A: Chem. 407 (2021), 113063.

[28] K.E. Ramohlola, M.J. Hato, G.R. Monama, E. Makhado, E.I. Iwuoha, K. D. Modibane, State-of-the-art advances and perspectives for electrocatalysis, in: Boddula R. Inamuddin, A. Asiri (Eds.), Methods For Electrocatalysis, Springer, Cham, 2020, pp. 311–352.

[29] K.E. Ramohlola, M. Masikini, S.B. Mdluli, G.R. Monama, M.J. Hato, K.M. Molapo, E.I. Iwuoha, K.D. Modibane, et al., Electrocatalytic hydrogen production properties of polyaniline doped with metal-organic frameworks, in: S. Kaneko, et al. (Eds.), Carbon-related Materials in Recognition of Nobel Lectures By Prof. Akira Suzuki in ICCE, Springer, Cham, 2017, pp. 373–389.

[30] K.E. Ramohlola, M. Masikini, S.B. Mdluli, G.R. Monama, M.J. Hato, K.M. Molapo, E.I. Iwuoha, K.D. Modibane, Electrocatalytic hydrogen evolution reaction of metal organic frameworks decorated with poly (3-aminobenzoic acid), Electrochim. Acta 246 (2017) 1174–1182.

[31] K.E. Ramohlola, M. Masikini, S.B. Mdluli, G.R. Monama, M.J. Hato, K.M. Molapo, E.I. Iwuoha, K.D. Modibane, Electrocatalytic hydrogen production properties of poly (3-aminobenzoic acid) doped with metal organic frameworks, Int. J. Elec. Sci. 12 (2017) 4392–4405.

[32] K.E. Ramohlola, G.R. Monana, M.J. Hato, K.D. Modibane, K.M. Molapo, M. Masikini, S.B. Mduli, E.I. Iwuoha, Polyaniline-metal organic framework nanocomposite as an efficient electrocatalyst for hydrogen evolution reaction, Compos. Part B 137 (2018) 129–139.

[33] G.R. Monama, M.J. Hato, K.E. Ramohlola, T.C. Maponya, S.B. Mdluli, K. M. Molapo, K.D. Modibane, E.I. Iwuoha, K. Makgopa, M.D. Teffu, Hierarchiral 4-tetranitro copper (II) phthalocyanine based metal organic framework hybrid composite with improved electrocatalytic efficiency towards hydrogen evolution reaction, Results Phys 15 (2019), 102564.

[34] G.R. Monama, S.B. Mdluli, G. Mashao, M.D. Makhafola, K.E. Ramohlola, K. M. Molapo, M.J. Hato, K. Makgopa, E.I. Iwuoha, K.D. Modibane, Palladium deposition on copper (II) phthalocyanine/metal organic framework composite and electrocatalytic activity of the modified electrode towards the hydrogen evolution reaction, Renew. Energy 119 (2018) 62–72.

[35] G.R. Monama, K.D. Modibane, K.E. Ramohlola, K.M. Molapo, M.J. Hato, M. D. Makhafola, G. Mashao, S.B. Mdluli, E.I. Iwuoha, Copper (II) phthalocyanine/metal organic framework electrocatalyst for hydrogen evolution reaction application, Inter. J. Hydrogen Energy. 44 (2019) 18891–18902.

[36] G. Mashao, K.E. Ramohlola, S.B. Mdluli, G.R. Monama, M.J. Hato, K. Makgopa, K. M. Molapo, M.E. Ramoroka, E.I. Iwuoha, K.D. Modibane, Zinc-based zeolitic benzimidazolate framework/polyaniline nanocomposite for electrochemical sensing of hydrogen gas, Mat. Chem. Phys 230 (2019) .287–.298.

[37] G. Mashao, K.D. Modibane, S.B. Mdluli, E.I. Iwuoha, M.J. Hato, K. Makgopa, K. M. Molapo, Polyaniline-cobalt benzimidazolate zeolitic metal-organic framework composite material for electrochemical hydrogen gas sensing, Electrocatalysis 10 (2019) 406–419.

[38] G.D. Sharma, D. Daphnomili, K.S.V. Gupta, T. Gayathri, S.P. Singh, P.A. Angaridis, T.N. Kitsopoulos, D. Tasise, A.G. Coutsolelos, Enhancement of power conversion efficiency of dye-sensitized solar cells by co-sensitization of zinc-porphyrin and thiocyanate-free ruthenium(II)-terpyridine dyes and graphene modified TiO_2 photoanode, RSC Adv 3 (2013), 22412–224.

[39] R. Rani, A. Deep, B. Mizaikoff, S. Sigh, Enhanced hydrothermal stability of Cu-MOF by post symthetic modification with amino acids, Vacuum 164 (2019) 449–457.

[40] P.M. Kumar, S. Badrinarayanan, M. Sastry, Nanocrystlline TiO_2 studied by optical, FTIR and X-ray photoelectrical spectroscopy: correlation to presence of surface states, Thin Solid Films 358 (2000) 122–130.

[41] N.R. Dhumal, M.P. Singh, J.A. Anderson, J. Kiefer, H.J. Kim, Molecular interactions of a Cu-based metal−organic framework with a confined imidazolium-based ionic liquid: a combined density functional theory and experimental vibrational, J. Phys. Chem. C. 120 (2016) 3295–3304.

[42] J.V.M. Zoccal, F.O. Arouca, J.A.S. Gonçalves, Synthesis and characterization of TiO2 nanoparticles by method Pichini, Seventh International Latin American,2009 Conference on Powder Technology, 2009 November 08-10, Atibaia, SP, Brazil.

[43] Y. Zhang, J. Guo, L. Shi, Y. Zhu, K. Hou, Y. Zheng, Z. Tang, Tunable chiral metal organic frameworks toward visible light–driven asymmetric catalysis, Sci. Adv. 3 (2017) 1162.

[44] N.M. Mahmoodi, J. Abdi, Nanoporous metal-organic framework (MOF-199): synthesis, characterization and photocatalytic degradation of basic blue 41, J. Microchem. 144 (2019) 436–442.

[45] M.C. So, G.P. Wiederrecht, J.E. Mondloch, J.T. Hupp, O.K. Farha, Metal–organic framework materials for light-harvesting and energy transfer, Chem. Commu. 51 (2015) 3501–3510.

[46] P. Data, M. Bialoglowski, K. Lyzwa, R. Bacewicz, P. Dluzewski, M. Lapkowskib, T. Gregorkiewicz, S. Podsiadlo, A.P. Monkman, Kesterite inorganic-organic heterojunction for solution processable solar cells, Electrochim. Acta. 201 (2016) 78–85.

[47] H.R. Zare, N. Nasirizadeh, M.M. Ardakani, Electrochemical properties of a tetrabromo- p-benzoquinone modified carbon paste electrode. Application to the simultaneous determination of ascorbic acid, dopamine and uric acid, J. Electr. Chem. 577 (2005) 25–33.

[48] A.V. Vinogradov, H. Zaake-Hertling, E. Hey-Hawkins, A.V. Agafonov, G. A. Seisenbaeva, V.G. Kessler, V.V. Vinogradov, The first depleted heterojunction TiO_2–MOF-based solar cell, Chem. Commun. 50 (2014) 10210–10213.

[49] J. Pei, Y.Z. Hao, H.J. Lv, B. Sun, Y.P. Li, Z.M. Guo, Optimizing the performance of TiO_2/P3HT hybrid solar cell by effective interfacial modification, Chem. Phys. Let. 644 (2016) 127–131.

[50] W. Yang M. Li, K. Pan, L. Guo, J. Wu, Z. Li, F. Yang, K. Lin, Zhou W, Surface engineering of mesoporous anatase titanium dioxide nanatubes for rapid spaechial charge separation on horizontal vertical dimensions and efficient solar-driven photocatalytic hydrogen evolution, J. Coll. Interfaces Sci 586 (2021) 75–83.

[51] K. munawar, M.A. Mansoor, W.J.B. Basirun, M. Masran, N.M. Huang, M. Mazhar, Single step fabrication of CuO-MnO-TiO_2 composite thin film with improved photoelectrochemichal response, RSC. Adv. 7 (2017) 15885.

[52] P.S. Ramaripa, K.M. Molapo, T.R. Somo, M.J.Hato M.D.Teffu, M.S. Maubane-Nkadimeng, K. Makgopa, E.I. Iwouha, K.D. Modibane, Photovoltaic Performance of Titaniumoxide/Metal Organic Framework, CRC. Press. Taylor & Francis, 2020, pp. 131–166. Chapter 5.

[53] M.D. Tyona, R.U. Osuji, P.U. Asogwa, S.B. Jambure, F.I. Ezema, Structural modification and band gap tailoring of zinc oxide thin films using copper impurities, J. Solid State Electrochem. 21 (2017) 2629–2638.